ARTICLES
PUBLISHED ONLINE: 27 MAY 2012 | DOI: 10.1038/NNANO.2012.72

nature nanotechnology

An oxygen reduction electrocatalyst based on carbon nanotube–graphene complexes

Yanguang Li[1], Wu Zhou[2,3], Hailiang Wang[1], Liming Xie[1], Yongye Liang[1], Fei Wei[4], Juan-Carlos Idrobo[3,2], Stephen J. Pennycook[3,2] and Hongjie Dai[1]*

Oxygen reduction reaction catalysts based on precious metals such as platinum or its alloys are routinely used in fuel cells because of their high activity. Carbon-supported materials containing metals such as iron or cobalt as well as nitrogen impurities have been proposed to increase scalability and reduce costs, but these alternatives usually suffer from low activity and/or gradual deactivation during use. Here, we show that few-walled carbon nanotubes, following outer wall exfoliation via oxidation and high-temperature reaction with ammonia, can act as an oxygen reduction reaction electrocatalyst in both acidic and alkaline solutions. Under a unique oxidation condition, the outer walls of the few-walled carbon nanotubes are partially unzipped, creating nanoscale sheets of graphene attached to the inner tubes. The graphene sheets contain extremely small amounts of irons originated from nanotube growth seeds, and nitrogen impurities, which facilitate the formation of catalytic sites and boost the activity of the catalyst, as revealed by atomic-scale microscopy and electron energy loss spectroscopy. Whereas the graphene sheets formed from the unzipped part of the outer wall of the nanotubes are responsible for the catalytic activity, the inner walls remain intact and retain their electrical conductivity, which facilitates charge transport during electrocatalysis.

There has been an intense search for efficient, durable and inexpensive alternatives to precious-metal electrocatalysts such as platinum (and its alloys) for the oxygen reduction reaction (ORR) in acidic media for proton-exchange membrane fuel cells[1–5]. For example, much has been done to produce metal- (for example, iron and cobalt) and nitrogen-containing catalysts by pyrolysing precursor compounds on a carbon support material such as carbon black or carbon nanotubes[6–10]. Problems plaguing such catalysts include insufficient activity and/or low stability against oxidation by peroxide intermediates, leading to catalyst deactivation[7]. Understanding the nature of ORR catalytic sites on the atomic scale using microscopy or spectroscopy, identifying the causes of instability, and designing catalysts with both optimal activity and stability for ORR in acidic solutions all remain outstanding challenges.

In principle, it should be possible to make use of the high degree of graphitization, electrical conductivity and corrosion resistance of carbon nanotubes to impart high stability to ORR electrocatalysts. However, the ORR activities of carbon-nanotube-based catalysts have been found to be low in acids. Nitrogen-doped multiwalled carbon nanotubes or aligned carbon nanotube arrays have been made by feeding in nitrogen precursors during the growth of nanotubes[11–15] or by annealing pre-oxidized nanotubes in NH_3 at elevated temperatures[16]. The resulting catalysts exhibited ORR activity in alkaline electrolytes[14,16,17] but poor activity in acids. So far, all nanotube-based ORR catalysts have exhibited inferior activities compared with those formed with carbon black and platinum/-carbon in acidic conditions, probably due to the relatively few catalytic sites formed on the carbon nanotubes. A possible approach to enhancing ORR activity is to introduce abundant defects and functional groups onto the carbon nanotubes to increase the number of catalytic sites. However, harsh oxidation conditions could lead to the loss of the structural integrity and high electrical conductivity of the nanotubes, a desirable property for charge transport during electrocatalysis. It would therefore be advantageous to identify a suitable strategy to afford abundant catalytic sites on carbon nanotubes while retaining the structure and electrical conductivity for producing advanced ORR electrocatalysts.

In this Article, we develop a new type of ORR electrocatalyst based on few-walled (two to three walls) carbon nanotube–graphene (NT–G) complexes. We identify a unique oxidation condition to produce abundant defects on the outer walls of the carbon nanotubes through partial unzipping of the outer walls and the formation of large amounts of nanoscale graphene sheets, attached to the intact inner walls of the nanotubes. The edge- and defect-rich graphene sheets facilitate the formation of catalytic sites for ORR on annealing in NH_3. Iron impurities and nitrogen doping are found to be responsible for the high ORR activity of the resulting NT–G complex catalyst. Indeed, in acidic solutions the catalyst exhibits high ORR activity and superior stability, and in alkaline solutions its ORR activity closely approaches that of platinum. We also use annular dark-field (ADF) imaging and electron energy loss (EEL) spectrum imaging in aberration-corrected scanning transmission electron microscopy (STEM) to investigate the chemical nature of the ORR catalytic sites on the atomic scale. Iron atoms are often found along the edges of the defective graphene sheets attached to the intact inner walls of few-walled nanotubes, and they often appear next to nitrogen atoms. This provides the first indication of the atomically resolved structure of the ORR catalyst.

Electrocatalyst preparation and characterization

Few-walled carbon nanotubes (with a high percentage of double-walled nanotubes and a small percentage of triple-walled nanotubes) grown from MgO-supported iron seeds by chemical vapour deposition[18] were oxidized in $KMnO_4/H_2SO_4$ solutions at 65 °C by systematically varying the concentration of $KMnO_4$ (see

[1]Department of Chemistry, Stanford University, Stanford, California 94305, USA, [2]Department of Physics and Astronomy, Vanderbilt University, Nashville, Tennessee 37235, USA, [3]Materials Science & Technology Division, Oak Ridge National Laboratory, Oak Ridge, Tennessee 37831, USA, [4]Department of Chemical Engineering, Tsinghua University, Beijing 100084, China. *e-mail: hdai@stanford.edu

© 2012 Macmillan Publishers Limited. All rights reserved.

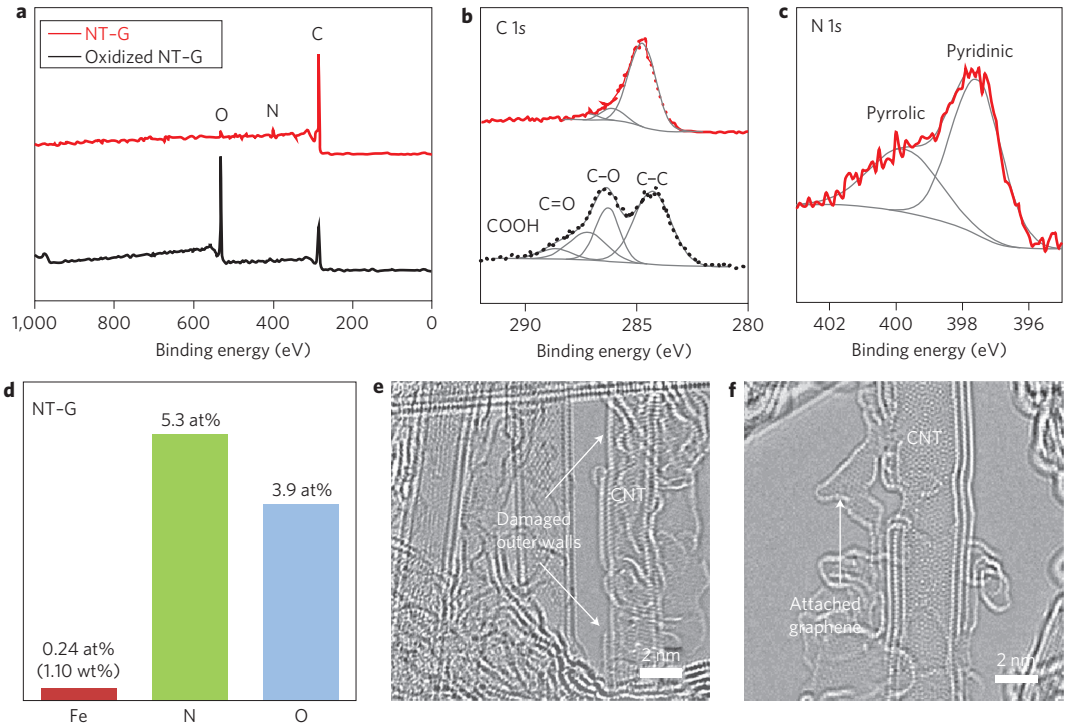

Figure 1 | Structural and compositional characterization of carbon nanotube–graphene complexes. a, XPS survey spectra of as-oxidized material (oxidized NT–G) and final catalyst (NT–G). **b**,**c**, High-resolution C 1s XPS spectra (**b**) and N 1s spectra (**c**) of as-oxidized material (oxidized NT–G, black) and final catalyst (NT–G, red). Oxidized NT–G is reduced and doped with nitrogen during the high-temperature ammonia annealing. **d**, Chart showing the percentages of iron, nitrogen and oxygen in the final NT–G material measured by ICP-MS and XPS. **e**,**f**, Aberration-corrected TEM images of the NT–G material, showing damaged outer walls and exfoliated graphene pieces attached to double- or triple-walled carbon nanotubes (CNTs).

Methods). A harsh oxidation condition ($KMnO_4$:carbon nanotube mass ratio ≈ 5) was identified to afford oxidized carbon nanotubes with partially unzipped outer walls and exfoliated graphene oxide pieces and nanoribbons (Supplementary Fig. S1a,b; the oxidized product is denoted 'oxidized NT–G'). The oxidation method uses a similar concentration of $KMnO_4$ oxidizer as used by Tour and co-workers for unzipping multiwalled nanotubes when producing oxidized graphene nanoribbons[19]. The defective nature of the oxidized material is evident from the high D/G ratio in Raman spectroscopy (Supplementary Fig. S1c). The average length of the oxidized tubes was determined to be on the order of several hundred nanometres from atomic force microscopy (AFM; Supplementary Fig. S1d). Based on X-ray photoelectron spectroscopy (XPS) analysis, a nominal 36 at% oxygen was measured in the as-oxidized material in the form of hydroxyl, carbonyl and carboxyl groups (Fig. 1a,b, black curves).

Subsequently, the water-soluble oxidized NT–G material was ultrasonicated, centrifuged to remove aggregates, then lyophilized and subjected to NH_3 annealing at 900 °C to afford the final product, denoted NT–G. X-ray photoelectron spectroscopy analysis revealed that most oxygen groups were removed by the annealing process (Fig. 1a). The NT–G material contains pyridinic and pyrrolic nitrogen species[20] with a nominal nitrogen level of ~5.3 at% (Fig. 1c). Nitrogen groups in the nanotubes result from reactions of NH_3 with oxygen functionalities[21] and other defects in the oxidized graphitic structures[22,23]. Inductively coupled plasma mass spectroscopy (ICP-MS) revealed an iron content of ~1.10 wt% (corresponding to 0.24 at%, Fig. 1d) in the final product, which is inherited from the metal impurities contained in the initial raw material (~3.7 wt%).

Figure 1e,f presents high-resolution aberration-corrected transmission electron microscopy (TEM) images of the NT–G material. The nanotubes are mostly two- to three-walled, with their outer walls damaged and exfoliated to form single-layered nanosized graphene pieces (<5 nm) or ribbon-like structures (Supplementary Fig. S1b) by the harsh oxidation process. These graphene structures exhibit abundant edges and are often found attached to nanotubes. Regions with intact inner walls on the exfoliated nanotubes are also frequently observed.

Electrocatalyst activity and durability

We performed cyclic voltammetry (CV) and rotating ring-disk electrode (RRDE) measurements in 0.1 M $HClO_4$ to assess the ORR activity of NT–G material that had been ultrasonically dispersed in a Nafion solution of H_2O/ethanol mixed solvent (Nafion-to-catalyst mass ratio, ~0.1) then deposited onto a glassy carbon working electrode. As a reference point, commercial 20 wt% platinum on Vulcan carbon black (Pt/C from E-tek) was measured for comparison[24–26]. The NT–G material exhibits a pronounced cathodic ORR peak at 0.75 V versus the reversible hydrogen electrode (RHE) when the electrolyte is saturated with O_2 (Fig. 2a). The high ORR activity is also gleaned from its onset potential (~0.89 V) and half-wave potential ($E_{1/2} \approx 0.76$ V) in the RRDE polarization curves (Fig. 2b). The mass activity of the NT–G catalyst at 0.80 V is 4.4 A g^{-1}, making it one of the most active ORR catalysts[7,27]. The H_2O_2 yield is less than 4% at all potentials, decreasing to ~2% at 0.2 V (Fig. 2b). Kinetic currents derived from the mass transport correction of the disk currents (Fig. 2c) show a Tafel slope of ~68 mV per decade at low currents, close to the ~70 mV per decade for the Pt/C catalyst. Similar to ORR catalysed by platinum, transfer of the first electron catalysed by NT–G is probably the rate-determining step, as indicated by the Tafel slope being close to $-2.303RT/\alpha F \approx 60$ mV per decade (R, T, α and F are the molar gas constant, absolute temperature, transfer coefficient and Faraday constant, respectively) at room temperature[28,29].

The NT–G catalyst shows markedly higher ORR catalytic activity than previous carbon-nanotube-based electrocatalysts in acidic

© 2012 Macmillan Publishers Limited. All rights reserved.

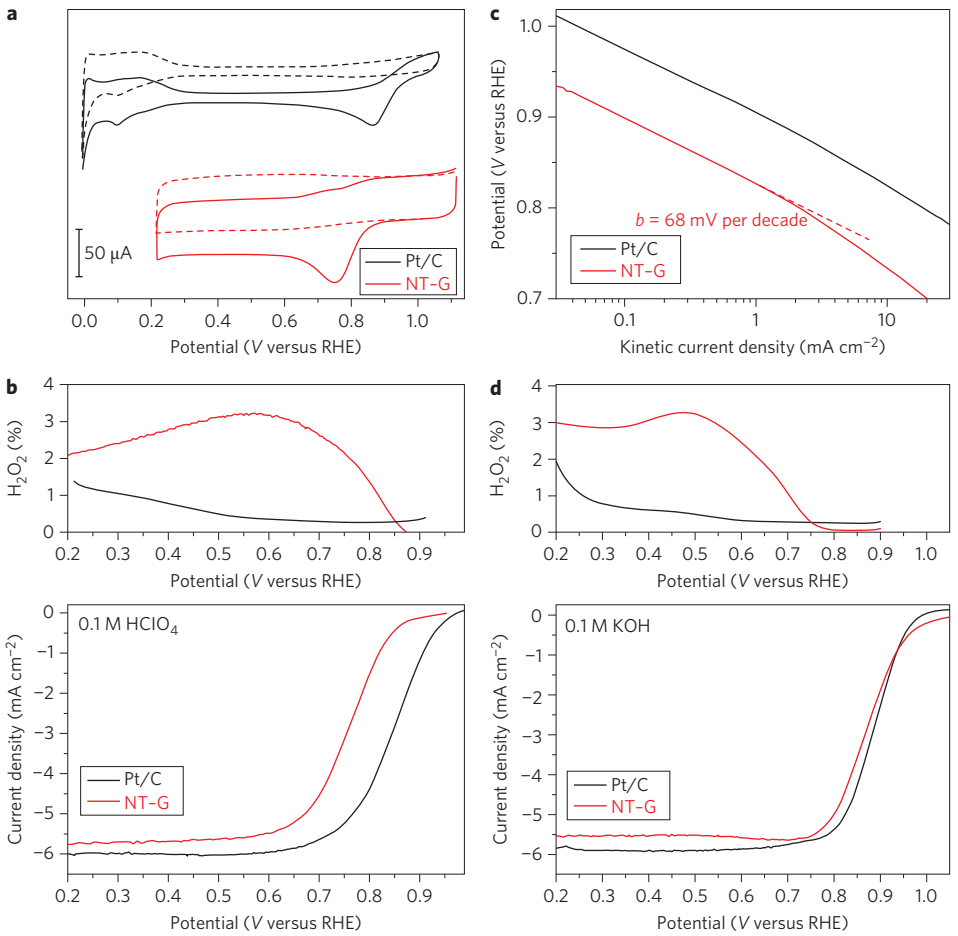

Figure 2 | Electrochemical characterization of the carbon nanotube–graphene ORR catalyst. a, CVs of commercial 20% Pt/C (black) and NT-G (red) catalysts in O_2-saturated (solid) or argon-saturated (dotted) 0.1 M $HClO_4$. **b**, RRDE polarization curves and peroxide yield of Pt/C (black) and NT-G (red) in O_2-saturated 0.1 M $HClO_4$. **c**, Kinetic current densities versus potential derived from the mass transport correction of the corresponding RRDE disk currents in **b**. **d**, RRDE polarization curves and peroxide yield of Pt/C (black) and NT-G (red) in O_2-saturated 0.1 M KOH. NT-G exhibits high ORR electrocatalytic activity in both acidic and alkaline electrolytes. For all the RRDE measurements, the loading of catalysts is 16 μg_{Pt} cm^{-2} for Pt/C and 0.485 mg cm^{-2} for NT-G. Electrode rotation speed, 1,600 r.p.m.; scan rate, 5 mV s^{-1}. Platinum data are collected from anodic sweeps.

media[11–14,30], with a more positive ORR onset potential (by >150 mV; Supplementary Table S1) and well-defined plateaux of diffusion-limiting currents in the RRDE polarization curves. In 0.1 M KOH electrolyte, the NT–G catalyst shows an ORR activity closely approaching that of Pt/C with an ORR onset potential >1.05 V (Fig. 2d).

We assessed the durability of the NT-G catalyst using the US Department of Energy's accelerated durability test protocol by cycling the catalysts between 0.6 and 1.0 V at 50 mV s^{-1} under argon and O_2 atmospheres, respectively[9,31]. After 8,000 continuous cycles, the half-wave potential $E_{1/2}$ exhibited a small negative shift of ~11 mV under argon cycling and ~17 mV under O_2 cycling (Fig. 3a–c), which compares favourably with most non-precious metal catalysts[9,31,32] and the Pt/C catalyst (>20 mV negative shift for Pt/C; see Fig. 3c and Supplementary Fig. S2). The NT–G catalyst was also exposed to fuel molecules (for example, methanol) for testing possible poisoning effects. For use in direct methanol fuel cells, ORR catalysts should exhibit satisfactory tolerance to the methanol that may pass across the membrane from the anode. We therefore measured the RRDE polarization curves in the presence of 0.5 M methanol, observing, as expected[1], a drastic decrease in the ORR activity of Pt/C (Fig. 3d). In contrast, the NT–G catalyst shows little activity loss (Fig. 3e), exhibiting excellent tolerance to methanol poisoning effects.

Identifying an optimal oxidation condition for the few-walled carbon nanotubes is key to the high activity of the carbon nanotubes–graphene ORR catalyst. We therefore investigated the effect of nanotube oxidation degree (using Hummers' oxidation method with a $KMnO_4$:carbon ratio varying from 1 to 8, or by using the reflux method in 3:1 v/v H_2SO_4:HNO_3; ref. 33) on the ORR electrocatalytic activity of the final product. We found that Hummers' oxidation with a $KMnO_4$:carbon ratio of 5 affords the most active ORR catalyst over other oxidation conditions (Supplementary Fig. S3). Transmission electron microscopy imaging revealed that the commonly used acid refluxing oxidation method[33] (Supplementary Fig. S3d) and also low degrees of Hummers' oxidation conditions (Supplementary Fig. S3a,b) fail to unzip the carbon nanotubes and produce few exfoliated graphene sheets of nanosize width. Excessive oxidation (with a $KMnO_4$:carbon ratio of ~8) destroys most nanotubes (Supplementary Fig. S3c) and eliminates the intact inner tubes that are desirable for hosting the graphene sheets containing active ORR sites and for facilitating the charge transport needed for ORR.

Furthermore, we found that our method can be generalized to produce highly active ORR catalysts with multiwalled carbon nanotubes (from C-NANO) as the starting material and by intentionally adding iron precursors to the nanotubes (Supplementary Fig. S4). Similar exfoliated nanosized graphene sheets attached

© 2012 Macmillan Publishers Limited. All rights reserved.

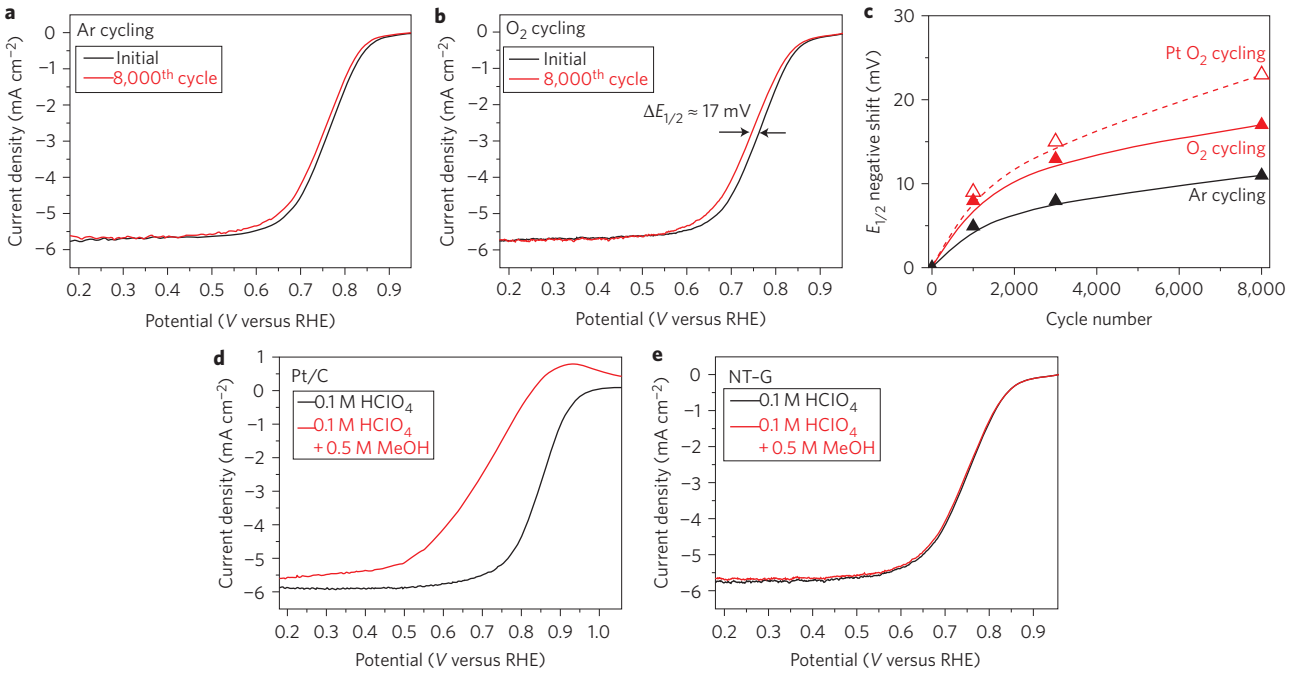

Figure 3 | Characterization of the durability and methanol tolerance of the NT–G ORR catalyst. a,**b**, RRDE polarization curves of the NT–G catalyst before and after 8,000 potential cycles in argon- or O_2-saturated 0.1 M $HClO_4$, respectively. Potential cycling was carried out between 0.6 and 1.0 V versus RHE at 50 mV s^{-1}. **c**, Negative shift of the NT–G half-wave potential ($E_{1/2}$) under argon or O_2 cycling compared with the Pt/C reference material under O_2 cycling. Little ORR activity loss is observed for NT–G during the accelerated durability test. **d**,**e**, RRDE polarization curves of Pt/C (**d**) and NT–G (**e**) in O_2-saturated 0.1 M $HClO_4$ with (red) or without (black) 0.5 M methanol. NT–G exhibits a dramatically enhanced tolerance to methanol compared with Pt/C.

to multiwalled nanotubes with intact inner tubes are also observed in aberration-corrected TEM experiments (Supplementary Fig. S4a,b). The existence of defective graphitic structures is evident from the high D/G ratio in Raman spectroscopic data (Supplementary Fig. S4c). Electrochemical RRDE polarization curves revealed the high ORR activity of such a catalyst with an onset potential of ~0.87 V and half-wave potential of ~0.73 V, which is only slightly less active than the NT–G catalyst based on predominantly double-walled nanotubes (Supplementary Fig. S4d). This result suggests the generality of producing highly active ORR catalysts based on properly oxidized NT–G complexes.

Role of iron and nitrogen impurities

We found that iron impurities in the raw carbon nanotube sample contribute to the high activity of the carbon nanotubes–graphene ORR electrocatalyst. Vigorous purification was performed to remove as many metal impurities as possible before oxidation and NH_3 annealing (see Methods). ICP-MS and XPS analysis of the final product based on the purified material (purified NT–G) revealed a substantial decrease in iron content to ~0.11 wt% (from ~1.1 wt% in NT–G), whereas the nitrogen and oxygen levels and percentages of pyridinic nitrogen were similar to those for NT–G ((Fig. 4a) Supplementary Fig. S5a). Raman and TEM characterizations revealed that purified NT–G also exhibits a similar degree of disorder in the graphitic structures to NT–G (Supplementary Fig. S5b,c). Importantly, however, the purification and iron removal step cause a large loss in ORR activity in purified NT–G (Fig. 4b,c), with an onset ORR potential ~100 mV more negative than NT–G (Fig. 4b,c), accompanied by a smaller RRDE disk current and higher percentage of peroxide generation (Fig. 4c).

To determine the role of iron in forming active ORR catalytic sites in the NT–G complex, we investigated the ORR activity of NT–G and purified NT–G in 0.1 M KOH containing 10 mM KCN (Fig. 4d and Supplementary Fig. S6). CN^- ions are known to coordinate strongly to iron and poison the iron-centred catalytic sites for ORR, as in the case of iron phthalocynanine catalysts[34,35]. In the presence of CN^-, the ORR onset potential of the NT–G catalyst decreases significantly by more than 100 mV, with a decrement in the diffusion-limiting current (Fig. 4d), suggesting blocking of the iron sites by CN^- ions and a reduction of the electron transfer number from four-electron. Interestingly, the purified NT–G material shows less activity loss in the presence of CN^-, exhibiting an ORR activity similar to the NT–G catalyst under CN^- blocking (Supplementary Fig. S6). A further comparison was made with metal-free nitrogen-doped graphene made by NH_3 annealing of graphene oxide at 900 °C (ref. 21). It is worth noting that the metal-free nitrogen-doped graphene is found to be much less ORR-active than iron-containing NT–G (especially in 0.1 M $HClO_4$), with lower diffusion-limited current and higher peroxide generation (Supplementary Fig. S7). However, nitrogen-doped graphene exhibits no appreciable ORR activity decrease in the presence of CN^- (Fig. 4d), suggesting no poisoning effects of CN^- on the nitrogen functionalities in the catalyst. Also important is the fact that the same NT–G material annealed in argon or vacuum without any NH_3 for nitrogen doping demonstrates very low ORR activity. These results suggest that both iron and nitrogen species are important to the high ORR electrocatalytic activity observed in the NT–G material.

To investigate the atomic distribution of iron and nitrogen in the NT–G catalyst, we performed STEM-ADF imaging (a technique sensitive to the atomic number Z)[36] in an aberration-corrected STEM, with simultaneous chemical mapping by EELS (ref. 37). The STEM analysis was performed on very thin regions of the sample, either from a single suspended nanotube (two to four atomic layers thick) or a suspended graphene layer attached to an isolated carbon nanotube (one to two layers thick). In this way, we ensured that we were imaging only the exposed surfaces of the sample, as well as unambiguously resolving single heavy dopant atoms and the carbon lattice. The bright-field STEM image (Fig. 5a) and corresponding ADF image (Fig. 5b) confirm nanosized graphene pieces attached to carbon nanotubes. Bright atoms

© 2012 Macmillan Publishers Limited. All rights reserved.

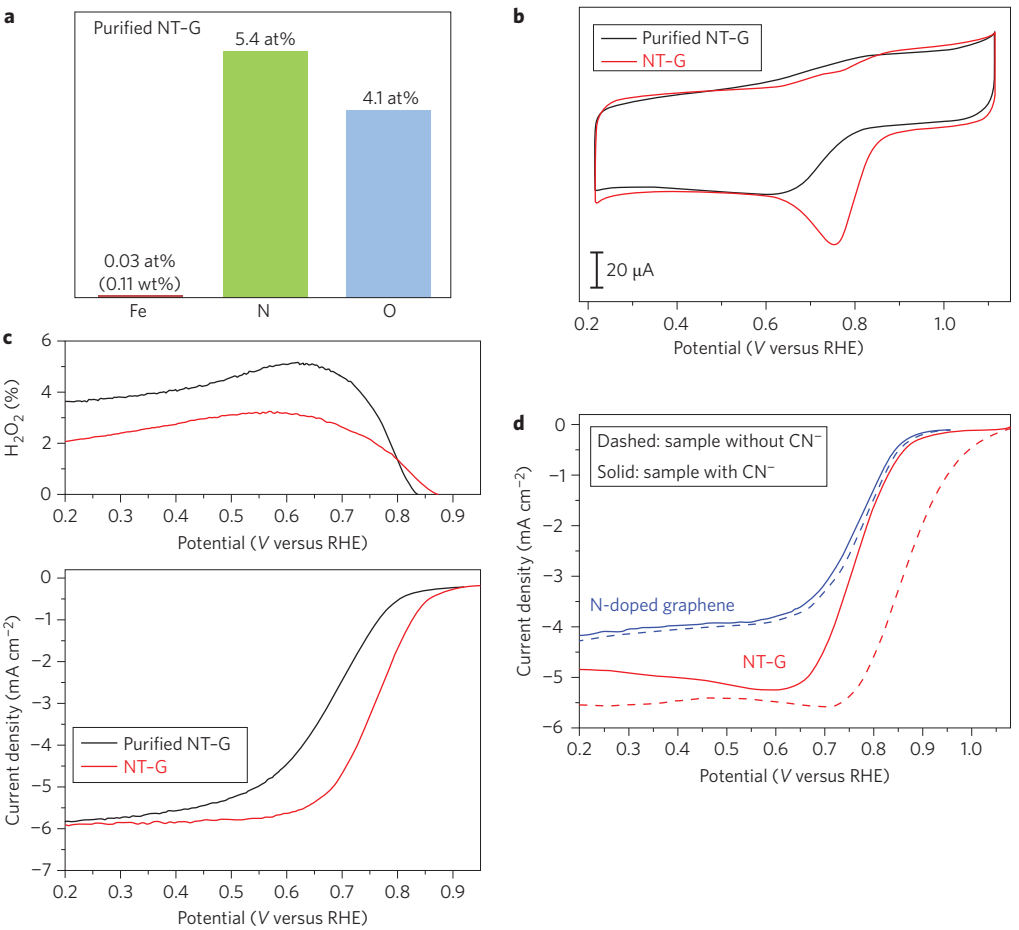

Figure 4 | Characterization of the role of iron in ORR catalysed by the NT–G material. a, Chart showing the percentages of iron, nitrogen and oxygen in purified NT–G determined by ICP-MS and XPS analysis. Compared with NT–G without intentional iron impurity removal, purified NT–G shows a substantial decrease in iron content. **b**,**c**, CV (**b**) and RRDE polarization curve and peroxide yield (**c**) of purified NT–G in comparison with NT–G without intentional iron impurity removal in O_2-saturated 0.1 M $HClO_4$. Purified NT–G exhibits a marked ORR activity loss due to iron removal. **d**, RRDE polarization curves for NT–G (red) and nitrogen-doped graphene (blue) in O_2-saturated 0.1 M KOH with (solid lines) or without (dashed lines) 10 mM CN^-. Exposure to CN^- ions blocks iron sites in the NT–G catalyst and reduces ORR activity; this CN^- poisoning effect is not observed for metal-free nitrogen-doped graphene.

dispersed over the graphitic carbon background are observed (Fig. 5b), corresponding to heavy elements. The atoms with the highest ADF contrast are identified by EELS analysis to be predominantly iron atoms (Fig. 5c). Some silicon impurities (source unknown) were also detected by EELS and show intermediate image contrast in Fig. 5b. The iron atoms are preferentially located on graphene pieces, especially at the edges (Fig. 5b and Supplementary Figs S8,S9). In contrast, iron atoms are rarely observed on the intact walls of the carbon nanotubes.

Elemental mapping by EELS imaging (Fig. 5d–g) was performed to determine the spatial relations between iron and nitrogen atoms on the NT–G complexes through simultaneous ADF imaging (Fig. 5d) and EELS elemental mapping of nitrogen (Fig. 5e) and iron (Fig. 5f) atoms. The data set was taken from the sample region highlighted in Fig. 5b. Bright atoms in the ADF image (Fig. 5d) correspond well with the EELS signals of iron (Fig. 5f). Nitrogen species were identified and mapped out by STEM-EELS (Fig. 5e) and overlaid with the iron signals (Fig. 5g and additional chemical mapping data sets in Supplementary Figs S8,S9). It was found that iron atoms on the graphene sheets are often adjacent or close to nitrogen atoms, suggesting possible Fe–N bonding. Further work is needed to resolve the chemical bonding configurations of single iron and nitrogen atoms in graphene lattices. To our knowledge, this is the first time that iron and nitrogen atoms have been imaged by ADF STEM and mapped out by atomic-scale EEL spectroscopic imaging for ORR electrocatalysts.

Many years ago, Yeager and co-workers proposed metal cations coordinated by pyridinic nitrogen atoms at defects of graphitic carbon as active ORR sites[7,8,38]. Despite intense investigations[35,38,39], the exact nature and structure of ORR active sites remained unclear and they have not been imaged at the atomic scale previously. It is possible that the NT–G material falls into the category of metal–nitrogen catalysts because of the observed iron and nitrogen atoms in the graphitic lattices as well as Fe–N proximity. The cyanide experiments also suggest that the high ORR activity of NT–G is due to iron-containing species, with the degree of ORR activity loss to CN^- blocking dependent on the iron level in the material (Supplementary Fig. S6). The iron species in our NT–G catalyst originate from the metal seed nanoparticles used in synthesizing the carbon nanotubes. It is possible that during the solution-phase oxidation step, iron nanoparticles are etched into Fe^{3+}, which is known to coordinate and bind to carboxylic acid groups[40] on the unzipped outer walls of nanotubes and graphene oxide pieces attached to nanotubes. On annealing, the iron species can react with NH_3 to form Fe–N moieties in the NT–G complex.

Conclusions

We have synthesized the first ORR electrocatalyst based on carbon nanotubes–graphene complexes, which exhibit a high activity,

© 2012 Macmillan Publishers Limited. All rights reserved.

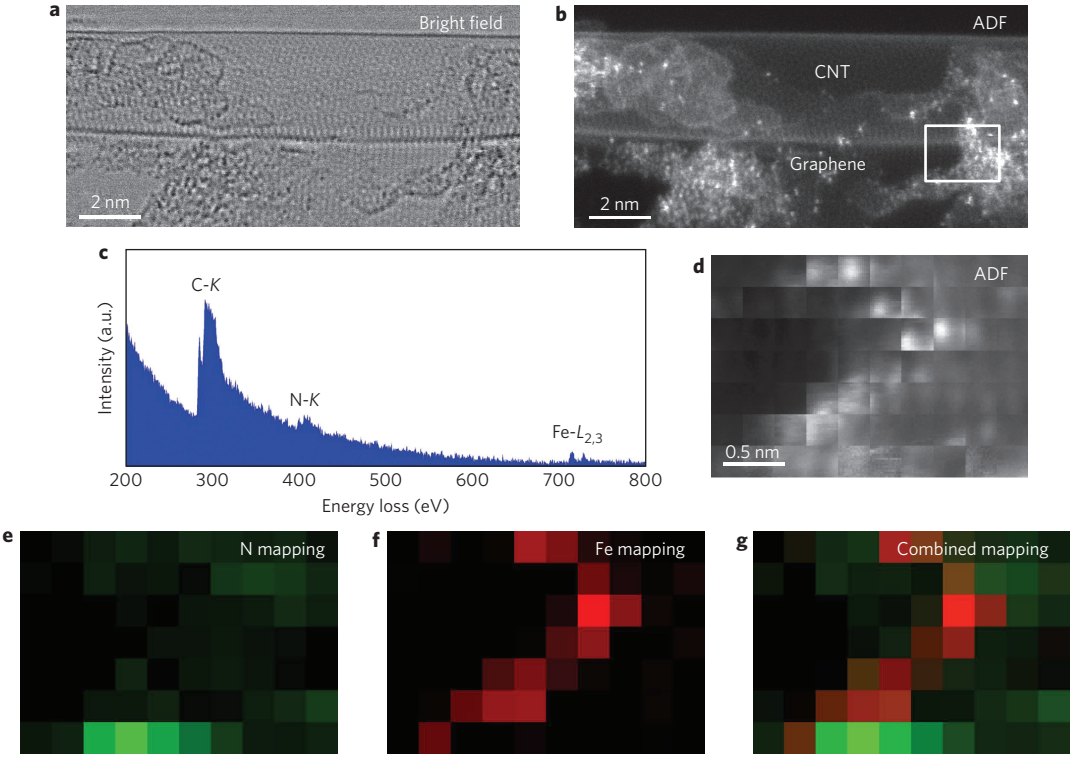

Figure 5 | Microscopy imaging and spectroscopic mapping of iron and nitrogen atoms on carbon nanotube–graphene complexes. a,**b**, Bright-field (**a**) and ADF STEM (**b**) images of a carbon nanotube partially covered with nanosized graphene pieces, showing many heavy atoms in the NT–G material (bright regions). **c**–**g**, The area marked by the white square in **b** is further characterized by EELS (**c**, spectrum summed over the area indicated), ADF intensity mapping (**d**), nitrogen EELS mapping (**e**), iron EELS mapping (**f**) and an overlaid iron and nitrogen EELS map (**g**). The ADF and EELS maps were recorded simultaneously. Interestingly, iron atoms are frequently observed on the edges of graphene sheets in close proximity to nitrogen species.

excellent tolerance to methanol and superior stability in comparison to other non-precious metal catalysts, in both acidic and alkaline solutions. The high ORR electrocatalytic activity and durability of the NT–G catalyst are attributed to a novel carbon-based structure formed by an optimal oxidation condition identified for few-walled carbon nanotubes. The oxidation method produces partially unzipped, damaged outer walls in the carbon nanotubes, with numerous small graphene oxide pieces attached to the outer walls. These structures present abundant edges and defect sites, which are responsible for the ORR catalytic activity. The less damaged or intact inner walls of the nanotubes are electrically conducting and highly stable against corrosion during ORR, maintaining the high electrical conductivity in the complex that is needed for sustaining efficient charge transport during electrocatalysis. Moreover, the high degree of graphitization of the carbon nanotubes, the exfoliated outer walls and the graphene pieces in the NT–G sample could be responsible for imparting high oxidative corrosion resistance to the catalytic sites and thus high durability to the carbon nanotubes–graphene ORR electrocatalyst. Furthermore, purified NT–G with the metal impurities largely removed affords significantly lower ORR activity. The NT–G catalyst shows a significant loss in activity on exposure to cyanide anions, suggesting that the high ORR activity stems from iron-containing catalytic sites. Using aberration-corrected STEM-ADF and EELS mapping techniques we have investigated the distribution of iron and nitrogen atoms on the atomic scale and frequently observed iron atoms on the edges of graphene sheets in close proximity to nitrogen species. The catalyst synthesis strategy we have shown here exploits novel carbon-based structures, and could represent a general approach to highly efficient and durable electrocatalysts for a range of important electrochemical reactions.

Methods

Materials synthesis. Oxidized NT–G was prepared using a modified Hummers' method. Few-walled carbon nanotubes (0.5 g) were dispersed in 20 ml of concentrated H_2SO_4 in a flask and continuously stirred at room temperature for 24 h. $KMnO_4$ (2.5 g) was added slowly to the solution while keeping the temperature of the solution to <35 °C. The solution was stirred for 1 h, then heated to 65 °C for another 1 h. The reaction was then quenched by pouring over ice, followed by the addition of 5 ml of 30% H_2O_2 solution. The solution was centrifuged at 8,000 r.p.m. The collected solid was washed with 5% HCl solution twice, redispersed in H_2O and dialysed until the pH was >3. The solution was transferred to a glass vial, vigorously sonicated for 30 min, then centrifuged at 5,000 r.p.m. for 5 min. Oxidized NT–G in the supernatant was collected for later use. To prepare NT–G, lyophilized oxidized NT–G powders were annealed in 2 torr of 10% NH_3/argon at 900 °C for 30 min. For nanotube purification (to remove metal impurities), raw carbon nanotubes were first calcined in air at 450 °C for 30 min. These were then sonicated in concentrated HCl for 1 h. After washing the acid away, nanotube powders were lyophilized and annealed in vacuum (<1 mtorr) at 1,100 °C for 1 h. Subsequent oxidation and annealing were carried out in the same way as described above to afford purified NT–G. This procedure was effective in removing some of the amorphous carbon and metal impurities[41].

Electrochemical measurements. NT–G catalyst (4 mg) and 8 μl of 5 wt% Nafion solution were dispersed in 0.80 ml of H_2O and 0.20 ml of ethanol by sonication for >1 h to form a homogeneous ink. The formulation was optimized to give the best catalyst dispersion. CV and RRDE studies were conducted in a home-built electrochemical cell using a saturated calomel electrode (calibrated and converted to RHE; see Supplementary Information) as the reference electrode and a graphite rod as the counter electrode. For CV, 5 μl of the catalyst ink was loaded onto a glassy carbon electrode (3 mm in diameter). For RRDE, 30 μl of the catalyst ink was loaded onto a RRDE electrode with 5.6 mm glassy carbon disk. Before the start of each measurement, the 0.1 M $HClO_4$ electrolyte was bubbled with O_2 for >10 min. A flow of O_2 was maintained over the electrolyte during the measurement to ensure continuous O_2 saturation. For all RRDE measurements, the electrode rotation speed was 1,600 r.p.m. (scan rate, 5 mV s^{-1}; platinum data collected from anodic sweeps).

Commercial 20 wt% platinum on Vulcan carbon black (Pt/C from E-tek) was measured for comparison. The catalyst ink was prepared as follows. Pt/C (3 mg) and 24 μl of 5 wt% Nafion solution were dispersed in 1.0 ml of ethanol by sonication for >1 h. Other experimental conditions were the same as for the NT–G catalyst, except that a platinum wire was used as the counter electrode.

© 2012 Macmillan Publishers Limited. All rights reserved.

Characterization. HRTEM images were collected on an aberration-corrected FEI TEAM 0.5. STEM imaging and EELS analysis were performed with a Nion UltraSTEM located at Oak Ridge National Laboratory, an aberration-corrected STEM equipped with a cold field-emission electron source and a corrector of third- and fifth-order aberrations, operating with a probe current of ~110 pA at 60 kV accelerating voltage. EEL spectra were collected using a Gatan Enfina spectrometer, with an EELS collection semi-angle of 48 mrad. Samples were prepared by drop-drying a diluted suspension of oxidized NT-G onto a SiN TEM grid, then annealing in NH_3 at 900 °C. XPS spectra were collected on an SSI S-Probe XPS spectrometer. Samples were prepared by drop-drying from ethanol suspensions onto silicon wafers. Raman spectra of the powder samples were recorded with a LabRAM HR Raman microscope with a laser excitation wavelength of 532 nm. ICP-MS analyses were performed on a Thermo Scientific XSERIES 2. Samples were first calcined at 600 °C for 2 h. The residues were dissolved in a concentrated HNO_3 solution before dilution to the 1–5 ppm level with ~2% acid for the measurement. AFM was carried out with a Vecco IIIa Nanoscope in tapping mode.

Received 9 January 2012; accepted 13 April 2012; published online 27 May 2012

References

1. Gewirth, A. A. & Thorum, M. S. Electroreduction of dioxygen for fuel-cell applications: materials and challenges. *Inorg. Chem.* **49,** 3557–3566 (2010).
2. Winter, M. & Brodd, R. J. What are batteries, fuel cells, and supercapacitors? *Chem. Rev.* **104,** 4245–4269 (2004).
3. Gasteiger, H. A., Kocha, S. S., Sompalli, B. & Wagner, F. T. Activity benchmarks and requirements for Pt, Pt-alloy, and non-Pt oxygen reduction catalysts for PEMFCs. *Appl. Catal. B* **56,** 9–35 (2005).
4. Wu, J. & Yang, H. Synthesis and electrocatalytic oxygen reduction properties of truncated octahedral Pt_3Ni nanoparticles. *Nano Res.* **4,** 72–82 (2011).
5. Lim, B., Jiang, M., Yu, T., Camargo, P. H. C. & Xia, Y. X. Nucleation and growth mechanisms for Pd–Pt bimetallic nanodendrites and their electrocatalytic properties. *Nano Res.* **3,** 69–80 (2010).
6. Bezerra, C. W. B. *et al.* A review of Fe-N/C and Co-N/C catalysts for the oxygen reduction reaction. *Electrochim. Acta* **53,** 4937–4951 (2008).
7. Jaouen, F. *et al.* Recent advances in non-precious metal catalysis for oxygen-reduction reaction in polymer electrolyte fuel cells. *Energy Environ. Sci.* **4,** 114–130 (2011).
8. Lefevre, M., Proietti, E., Jaouen, F. & Dodelet, J-P. Iron-based catalysts with improved oxygen reduction activity in polymer electrolyte fuel cells. *Science* **324,** 71–74 (2009).
9. Wu, G., More, K. L., Johnston, C. M. & Zelenay, P. High-performance electrocatalysts for oxygen reduction derived from polyaniline, iron, and cobalt. *Science* **332,** 443–447 (2011).
10. Pylypenko, S., Mukherjee, S., Olson, T. S. & Atanassov, P. Non-platinum oxygen reduction electrocatalysts based on pyrolyzed transition metal macrocycles. *Electrochim. Acta* **53,** 7875–7883 (2008).
11. Yang, J., Liu, D-J., Kariuki, N. N. & Chen, L. X. Aligned carbon nanotubes with built-in FeN_4 active sites for electrocatalytic reduction of oxygen. *Chem. Commun.* 329–331 (2008).
12. Xiong, W. *et al.* 3-D carbon nanotube structures used as high performance catalyst for oxygen reduction reaction. *J. Am. Chem. Soc.* **132,** 15839–15841 (2010).
13. Kundu, S. *et al.* Electrocatalytic activity and stability of nitrogen-containing carbon nanotubes in the oxygen reduction reaction. *J. Phys. Chem. C* **113,** 14302–14310 (2009).
14. Geng, D. *et al.* Non-noble metal oxygen reduction electrocatalysts based on carbon nanotubes with controlled nitrogen contents. *J. Power Sources* **196,** 1795–1801 (2011).
15. Wiggins-Camacho, J. D. & Stevenson, K. J. Mechanistic discussion of the oxygen reduction reaction at nitrogen-doped carbon nanotubes. *J. Phys. Chem. C* **115,** 20002–20010 (2011).
16. Nagaiah, T. C., Kundu, S., Bron, M., Muhler, M. & Schuhmann, W. Nitrogen-doped carbon nanotubes as a cathode catalyst for the oxygen reduction reaction in alkaline medium. *Electrochem. Commun.* **12,** 338–341 (2010).
17. Gong, K., Du, F., Xia, Z., Durstock, M. & Dai, L. Nitrogen-doped carbon nanotube arrays with high electrocatalytic activity for oxygen reduction. *Science* **323,** 760–764 (2009).
18. Ning, G., Liu, Y., Wei, F., Wen, Q. & Luo, G. Porous and lamella-like Fe/MgO catalysts prepared under hydrothermal conditions for high-yield synthesis of double-walled carbon nanotubes. *J. Phys. Chem. C* **111,** 1969–1975 (2007).
19. Kosynkin Dmitry, V. *et al.* Longitudinal unzipping of carbon nanotubes to form graphene nanoribbons. *Nature* **458,** 872–876 (2009).
20. Wang, H., Cote, R., Faubert, G., Guay, D. & Dodelet, J. P. Effect of the pre-treatment of carbon black supports on the activity of Fe-based electrocatalysts for the reduction of oxygen. *J. Phys. Chem. B* **103,** 2042–2049 (1999).
21. Li, X. *et al.* Simultaneous nitrogen doping and reduction of graphene oxide. *J. Am. Chem. Soc.* **131,** 15939–15944 (2009).
22. Jaouen, F., Serventi, A. M., Lefevre, M., Dodelet, J-P. & Bertrand, P. Non-noble electrocatalysts for O_2 reduction: how does heat treatment affect their activity and structure? Part II. Structural changes observed by electron microscopy, Raman, and mass spectroscopy. *J. Phys. Chem. C* **111,** 5971–5976 (2007).
23. Wang, X. *et al.* N-doping of graphene through electrothermal reactions with ammonia. *Science* **324,** 768–771 (2009).
24. Garsany, Y., Baturina, O. A., Swider-Lyons, K. E. & Kocha, S. S. Experimental methods for quantifying the activity of platinum electrocatalysts for the oxygen reduction reaction. *Anal. Chem.* **82,** 6321–6328 (2010).
25. Gong, K. *et al.* Platinum-monolayer electrocatalysts: palladium interlayer on IrCo alloy core improves activity in oxygen-reduction reaction. *J. Electroanal. Chem.* **649,** 232–237 (2010).
26. Lima, F. H. B. *et al.* Catalytic activity-*d*-band center correlation for the O_2 reduction reaction on platinum in alkaline solutions. *J. Phys. Chem. C* **111,** 404–410 (2007).
27. Meng, H., Jaouen, F., Proietti, E., Lefevre, M. & Dodelet, J-P. pH-effect on oxygen reduction activity of Fe-based electro-catalysts. *Electrochem. Commun.* **11,** 1986–1989 (2009).
28. Anderson, A. B. & Sidik, R. A. Oxygen electroreduction on Fe^{II} and Fe^{III} coordinated to N_4 chelates. Reversible potentials for the intermediate steps from quantum theory. *J. Phys. Chem. B* **108,** 5031–5035 (2004).
29. Medard, C., Lefevre, M., Dodelet, J. P., Jaouen, F. & Lindbergh, G. Oxygen reduction by Fe-based catalysts in PEM fuel cell conditions: activity and selectivity of the catalysts obtained with two Fe precursors and various carbon supports. *Electrochim. Acta* **51,** 3202–3213 (2006).
30. Yu, D., Zhang, Q. & Dai, L. Highly efficient metal-free growth of nitrogen-doped single-walled carbon nanotubes on plasma-etched substrates for oxygen reduction. *J. Am. Chem. Soc.* **132,** 15127–15129 (2010).
31. Wu, G. *et al.* Titanium dioxide-supported non-precious metal oxygen reduction electrocatalyst. *Chem. Commun.* **46,** 7489–7491 (2010).
32. Li, X., Liu, C., Xing, W. & Lu, T. Development of durable carbon black/titanium dioxide supported macrocycle catalysts for oxygen reduction reaction. *J. Power Sources* **193,** 470–476 (2009).
33. Esumi, K., Ishigami, M., Nakajima, A., Sawada, K. & Honda, H. Chemical treatment of carbon nanotubes. *Carbon* **34,** 279–281 (1996).
34. Gupta, S., Fierro, C. & Yeager, E. The effects of cyanide on the electrochemical properties of transition-metal macrocycles for oxygen reduction in alkaline-solutions. *J. Electroanal. Chem.* **306,** 239–250 (1991).
35. Thorum, M. S., Hankett, J. M. & Gewirth, A. A. Poisoning the oxygen reduction reaction on carbon-supported Fe and Cu electrocatalysts: evidence for metal-centered activity. *J. Phys. Chem. Lett.* **2,** 295–298 (2011).
36. Krivanek, O. L. *et al.* Atom-by-atom structural and chemical analysis by annular dark-field electron microscopy. *Nature* **464,** 571–574 (2010).
37. Hunt, J. A. & Williams, D. B. Electron energy-loss spectrum-imaging. *Ultramicroscopy* **38,** 47–73 (1991).
38. Scherson, D. A. *et al.* *In situ* and *ex situ* Moessbauer spectroscopy studies of iron phthalocyanine adsorbed on high surface area carbon. *J. Phys. Chem.* **87,** 932–943 (1983).
39. Lefevre, M., Dodelet, J. P. & Bertrand, P. Molecular oxygen reduction in PEM fuel cells: evidence for the simultaneous presence of two active sites in Fe-based catalysts. *J. Phys. Chem. B* **106,** 8705–8713 (2002).
40. Thomas, L. A. *et al.* Carboxylic acid-stabilized iron oxide nanoparticles for use in magnetic hyperthermia. *J. Mater. Chem.* **19,** 6529–6535 (2009).
41. Wu, C., Li, J., Dong, G. & Guan, L. Removal of ferromagnetic metals for the large-scale purification of single-walled carbon nanotubes. *J. Phys. Chem. C* **113,** 3612–3616 (2009).

Acknowledgements

This work was supported in part by a Stinehart Grant for Energy Research at Stanford from the Stanford Precourt Institute for Energy, Intel and NCEM at Lawrence Berkeley Laboratory, which was supported by the US DOE (DE-AC02-05CH11231). W.Z. was supported by the NSF (DMR-0938330). J-C.I. was supported by Oak Ridge National Laboratory's Shared Research Equipment (ShaRE) User Facility, which is sponsored by the Office of Basic Energy Sciences, US Department of Energy. S.J.P. was supported by the Basic Energy Sciences programme of the Materials Sciences and Engineering Division of the US DOE.

Author contributions

Y.Li and H.D. conceived the project and designed the experiments. W.Z., J-C.I. and S.J.P. conducted ADF and EELS studies. F.W. synthesized carbon nanotubes. Y.Li, H.W., L.X. and Y.Liang performed catalyst preparation, structural characterizations and electrochemical measurements. Y.Li, W.Z., H.W., L.X., Y.Liang, F.W., J-C.I., S.J.P. and H.D. analysed the data. Y.Li and H.D. co-wrote the paper. All authors discussed the results and commented on the manuscript.

Additional information

The authors declare no competing financial interests. Supplementary information accompanies this paper at www.nature.com/naturenanotechnology. Reprints and permission information is available online at http://www.nature.com/reprints. Correspondence and requests for materials should be addressed to H.D.

© 2012 Macmillan Publishers Limited. All rights reserved.